



Article

Nanocrystalline ZnSnN₂ Prepared by Reactive Sputtering, Its Schottky Diodes and Heterojunction Solar Cells

Fan Ye *, Rui-Tuo Hong †, Yi-Bin Qiu †, Yi-Zhu Xie, Dong-Ping Zhang, Ping Fan and Xing-Min Cai *

Key Laboratory of Optoelectronic Devices and Systems of Ministry of Education and Guangdong Province, and Shenzhen Key Laboratory of Advanced Thin Films and Applications, College of Physics and Optoelectronic Engineering, Shenzhen University, Shenzhen 518060, China

* Correspondence: yefan@szu.edu.cn (F.Y.); caixm@szu.edu.cn (X.-M.C.)

† These authors contributed equally to this work.

Abstract: Abstract ZnSnN₂ has potential applications in photocatalysis and photovoltaics. However, the difficulty in preparing nondegenerate ZnSnN₂ hinders its device application. Here, the preparation of low-electron-density nanocrystalline ZnSnN₂ and its device application are demonstrated. Nanocrystalline ZnSnN₂ was prepared with reactive sputtering. Nanocrystalline ZnSnN₂ with an electron density of approximately 10¹⁷ cm⁻³ can be obtained after annealing at 300 °C. Nanocrystalline ZnSnN₂ is found to form Schottky contact with Ag. Both the current *I* vs. voltage *V* curves and the capacitance *C* vs. voltage *V* curves of these samples follow the related theories of crystalline semiconductors due to the limited long-range order provided by the crystallites with sizes of 2–10 nm. The *I*–*V* curves together with the nonlinear *C*⁻²–*V* curves imply that there are interface states at the Ag-nanocrystalline ZnSnN₂ interface. The application of nanocrystalline ZnSnN₂ to heterojunction solar cells is also demonstrated.

Keywords: ZnSnN₂; nanocrystalline; Schottky diode; heterojunction; solar cell



Citation: Ye, F.; Hong, R.-T.; Qiu, Y.-B.; Xie, Y.-Z.; Zhang, D.-P.; Fan, P.; Cai, X.-M. Nanocrystalline ZnSnN₂ Prepared by Reactive Sputtering, Its Schottky Diodes and Heterojunction Solar Cells. *Nanomaterials* **2023**, *13*, 178. <https://doi.org/10.3390/nano13010178>

Academic Editor: Shunri Oda

Received: 14 November 2022

Revised: 15 December 2022

Accepted: 26 December 2022

Published: 30 December 2022



Copyright: © 2022 by the authors. Licensee MDPI, Basel, Switzerland. This article is an open access article distributed under the terms and conditions of the Creative Commons Attribution (CC BY) license (<https://creativecommons.org/licenses/by/4.0/>).

1. Introduction

The family of Zn-IV-N₂ (IV = Si, Ge and Sn) is an analogue of the III nitrides [1]. As a member of this family, ZnSnN₂ has many advantages, which include a direct band gap, earth-abundance of constituent elements, no toxicity, a high absorption coefficient, a low fabrication cost, etc. [1–6]. These make ZnSnN₂ a highly competent candidate in photocatalytic, photovoltaic and light-emitting applications. Recent theoretical work shows that the photon-to-electron conversion efficiency of ZnSnN₂/CuCrO₂ heterojunction solar cells is approximately 22% [2].

ZnSnN₂ has been fabricated by various methods such as sputtering [3–14], molecular beam epitaxy (MBE) [15], high pressure metathesis reaction [16] and vapor-liquid-solid growth [17]. During the preparation of ZnSnN₂, Sn atoms can easily occupy the positions of Zn atoms, and this results in the formation of the intrinsic antisite defect Sn_{Zn} which is a divalent donor and which almost has the lowest formation energy in ZnSnN₂ [18,19]. Therefore, the antisite defect Sn_{Zn} is considered to be the major donor in most cases, and the prepared ZnSnN₂ usually has a very high density of approximately 10¹⁹ cm⁻³. Preparing ZnSnN₂ with an electron density of approximately or below 10¹⁷ cm⁻³ is still challenging due to the facile formation of the donor defect Sn_{Zn}.

Compared with its polycrystalline, crystalline or microcrystalline counterparts [3–17], nanocrystalline ZnSnN₂ whose crystalline grains or crystallites are smaller than 10 nm has never been studied. In this paper, we approach the high electron density problem of ZnSnN₂ with nanocrystallization. We show that nanocrystalline ZnSnN₂ with crystallites of approximately 2 nm in the amorphous matrix can be deposited by sputtering an alloy target of Zn and Sn (the Zn/Sn atomic ratio to be 3:1) in an atmosphere of N₂ and Ar. Annealing at 300 °C makes the reactively deposited ZnSnN₂ turn *n*-type conductive with an electron

density of approximately 10^{17} cm^{-3} and the annealed ZnSnN_2 remains nanocrystalline with a grain size of 2–10 nm. The device applications, such as Ag- ZnSnN_2 Schottky diodes and Cu_2O - ZnSnN_2 heterojunction solar cells, are studied.

2. Materials and Methods

2.1. Preparation and Characterization of ZnSnN_2

Reactive radio frequency (RF) magnetron sputtering was used to deposit the samples. The substrates were K9 glasses. The substrates were ultrasonically cleaned in acetone, ethanol and deionized water, and the washing time in each liquid was 15 min. The target was the alloy of Zn (99.99%) and Sn (99.99%), with the Zn/Sn atomic ratio to be 3:1, and the gases were Ar (99.99%) and N_2 (99.999%). The flow rate of Ar was 20 standard cubic centimeters per min (sccm), and that of N_2 was 6 sccm. The base pressure of the sputtering chamber was 5.4×10^{-4} Pa. During sputtering, the chamber pressure was 5 Pa and the RF sputtering power was 35 W. The substrates rotated with the substrate holder at 0.6π rad/s. Before film deposition, the target was sputtered for 5 min to clean the surface. The time for film deposition was 60 min. Some deposited samples were annealed for 1 h in a vacuum chamber in the flow of Ar (20 sccm) and at a pressure of 5 Pa. The annealing temperatures were 300 °C, 350 °C, 400 °C and 450 °C.

The films without annealing or annealed at different temperatures were characterized with X-ray diffraction (XRD, D/max 2500 PC, 18 kW, Cu $K\alpha$ radiation) and transmission electron microscopy (TEM, FEI Titan Cubed Themis G2 300). The samples for TEM observation were prepared by using the mechanical stripping method. The film thickness was measured with the surface profiler (Veeco Dektak 3ST), and the surface of the samples was characterized with scanning electron microscopy (SEM, Supra55 Sapphire). The samples were also characterized with atomic force microscopy (AFM, Oxford Instrument, MFP-3D Infinity, noncontact mode), room temperature Hall effect (HL 5500 PC, Van der Pauw electrode was used, and melted alloy of In and Sn was dropped at the four corners of a square sample to act as the electrodes) as well as X-ray photoelectron spectroscopy (XPS, Thermo Fisher, Thermo escalab 250Xi, Al $K\alpha = 1486.6$ eV; The C 1 s was calibrated to be 284.8 eV; the calculation of the atomic ratio is elaborated elsewhere [14]). The Seebeck coefficient S_e of the samples was measured with $\Delta V / \Delta T$ where ΔV is the voltage difference (ΔV is obtained with a voltmeter (Keithley 2400)) and ΔT is the temperature difference between the hot side and the cold side.

2.2. Preparation and Characterization of the Schottky Diodes and Heterojunctions

The steps to prepare the Schottky diodes with the structure of Ag/ITO/ ZnSnN_2 /Ag (ITO refers to indium tin oxide, and its resistivity is approximately $6.22 \times 10^{-4} \Omega \cdot \text{cm}$) are as follows (Supplementary Materials Figure S1): ZnSnN_2 was first deposited on ITO (whose substrate is glass) without annealing, and the thickness was 95 nm. During film deposition, some surface area of the ITO was covered with a mask in order to produce electrodes later. Secondly, a silver paste of $0.1 \text{ cm} \times 0.1 \text{ cm}$ was dropped on ZnSnN_2 and the surface of ITO to act as electrodes. To compare the effect of annealing, ZnSnN_2 deposited on ITO under the same conditions was annealed for 1 h at 300 °C in the flow of Ar before making the electrodes. During annealing, the vacuum pressure was also 5 Pa, and then the second step of dropping silver paste was repeated to produce electrodes for another Schottky diode.

To prepare Cu_2O - ZnSnN_2 heterojunctions (Supplementary Materials Figure S1), Cu_2O was first deposited on ITO with reactive DC sputtering (part of the ITO was also masked for making an electrical connection later). The sputtering voltage and current were 289 V and 35 mA. The target was copper (99.999%), and the gases were Ar (30 sccm) and O_2 (1.8 sccm). The work pressure was 0.6 Pa, and the substrate temperature was 400 °C. The sputtering time was 10 h, and the thickness of Cu_2O was 1672 nm (to obtain the electrical properties of Cu_2O , Cu_2O was also deposited on K9 glass, and Hall measurements showed that Cu_2O is *p*-type conductive with a hole density of $1.02 \times 10^{15} \text{ cm}^{-3}$). After Cu_2O cooled to room temperature naturally, ZnSnN_2 was deposited on Cu_2O and the parameters were the same

as those mentioned previously except that the sputtering time was 3 h here (the thickness of ZnSnN₂ was 236 nm here). Silver paste was dropped on the surface of ITO and ZnSnN₂ to produce one solar cell with the structure of Ag\ITO\Cu₂O\ZnSnN₂\Ag. Additionally, with silver paste dropped on the surface of ITO to produce an electrode, Au was evaporated on ZnSnN₂ to produce another solar cell with the structure of Ag\ITO\Cu₂O\ZnSnN₂\Au. The base pressure for evaporating Au was 5×10^{-4} Pa. Au wire (99.999%) was heated first with a current of 75 A for 10 min and then at a current of 90 A for 5 min. The solar cells had an area of 0.04 cm².

The current *I*-voltage *V* curves of the devices were measured at room temperature with a source measurement unit instrument (Keithley Standard Series 2400). The capacitance *C*-voltage *V* curves of the devices were measured at room temperature with a semiconductor characterization system (Keithley 4200-SCS), and the frequency used was 10 kHz. For the Schottky diodes, the forward-bias is defined as the state at which the Ag electrode, in direct contact with the ZnSnN₂ layer, is connected with the anode of the voltage. The solar cells are forward-biased when the electrostatic potential of Cu₂O is higher than that of ZnSnN₂. The current density-voltage *V* curves of the two Cu₂O-ZnSnN₂ heterojunction solar cells were measured at room temperature with a multi-meter (Keithley, 2400 Series) under AM1.5 light illumination (which is from an AAA solar simulator with the intensity calibrated to 100 mW/cm² through a Si reference cell).

3. Results and Discussion

The XRD patterns of the samples deposited at 35 W and room temperature (the substrates were not intentionally heated) without annealing and those deposited at the same conditions but annealed at 300–450 °C are presented in Figure 1a. No diffraction peaks were observed in the XRD patterns of these samples. The samples deposited at 35 W and room temperature without annealing were amorphous, and they were still amorphous after annealing at 300–450 °C. In our equipment, when the sputtering power and other parameters were kept unchanged, the samples deposited at the substrate temperature of 100–300 °C became polycrystalline, and the preferred orientation changed when the substrate temperature was over 200 °C (Figure 1b, also Supplementary Materials Figure S2). However, when the sputtering power is 50 W, even the samples deposited at room temperature are polycrystalline (Figure 1c; also Supplementary Materials Figure S3). This implies that relatively higher sputtering power favors crystallization, and this agrees with F. Al-njiman et al., who showed that polycrystalline ZnSnN₂ can be deposited without heating the substrate intentionally [7]. Though the samples deposited at the substrate temperature of 100–300 °C were polycrystalline, the samples deposited at room temperature and then annealed at 300 °C or above after deposition remained amorphous, and post-deposition annealing failed to make the amorphous samples turn to polycrystalline. This is different from amorphous ZnSnN₂ prepared by direct current sputtering, which turns into polycrystalline after annealing [12]. Therefore, amorphous ZnSnN₂ is relatively stable since it remains amorphous even if the post-deposition annealing temperature is higher than 300 °C. It is reported that reducing the Zn/Sn ratio to a certain degree leads to microcrystalline and amorphous ZnSnN₂ [13], while in our work, reducing the substrate temperature to fabricate amorphous ZnSnN₂ was used. Later, we will show that both the ZnSnN₂ samples without annealing and the ZnSnN₂ samples annealed at 300 °C are actually nanocrystalline with crystallites of 2–10 nm. The Raman scattering spectra of these samples show that the obtained ZnSnN₂ is phonon-glass-like (Supplementary Materials Figure S4).

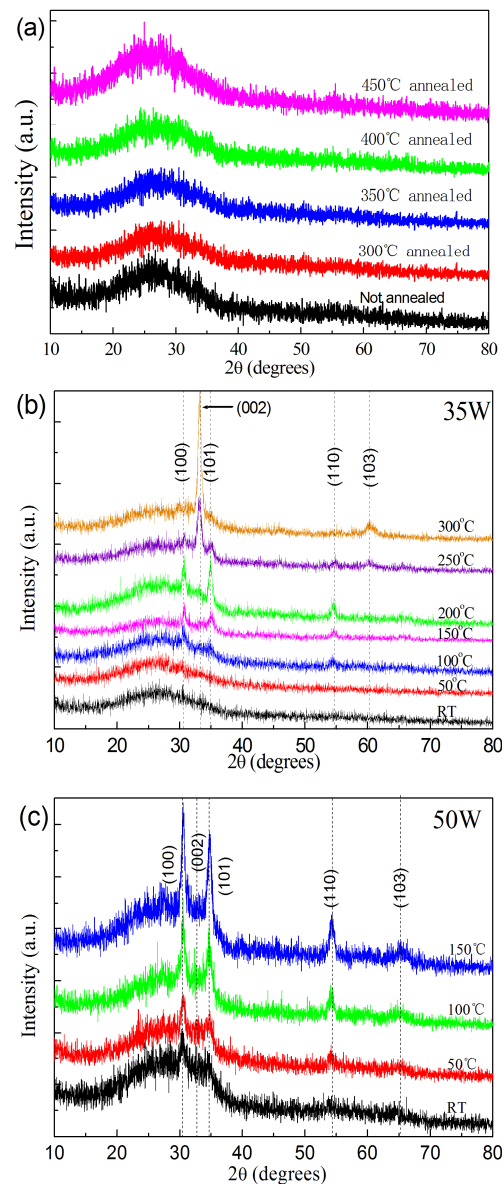


Figure 1. (a) XRD patterns of the samples without annealing or annealed at 300–450 °C; (b) XRD patterns of the samples deposited at 35 W and under different substrate temperatures; (c) XRD patterns of the samples deposited at 50 W and under different substrate temperatures.

The transmittance (T_r) and reflectance (R) spectra of the samples were measured with an UV/VIS spectrophotometer. The absorption coefficient α is equal to $t^{-1} \ln[(1 - R)T_r^{-1}]$, where t is the thickness of the film (cm). The thickness of the films before and after annealing is approximately 95 nm. For semiconductors with a direct band gap, the relation between the absorption coefficient α and the optical band gap E_g^{opt} is as follows:

$$(\alpha h\nu)^2 = A(h\nu - E_g^{opt}), \quad (1)$$

where A is a constant, h is the Planck constant and ν is the photon frequency. The optical bandgap E_g^{opt} can be obtained by extrapolating the linear region to intercept the $h\nu$ axis in the plot of $(\alpha h\nu)^2$ vs. $h\nu$. With the assumption that nanocrystalline ZnSnSn₂ has a direct band gap, the optical bandgap E_g^{opt} of all the samples can be obtained, as shown in Figure 2. The optical bandgap of nanocrystalline ZnSnSn₂ is approximately 2.75 eV, which is larger than the experimental band gap of crystalline or polycrystalline ZnSnSn₂

(0.94–2.38 eV [15,20]), and this is in agreement with the fact that the band gap of amorphous Si is larger than its crystalline counterparts. The optical band gaps of the samples annealed at 300 °C, 350 °C, 400 °C and 450 °C were 2.40 eV, 2.35 eV, 2.11 eV and 2.15 eV, respectively. In amorphous and microcrystalline ZnSnN₂ fabricated by reducing the Zn/Sn ratio, the optical bandgap is also approximately 2.53–2.59 eV [13], and our work agrees with this. It has been found that annealing reduces the band gap.

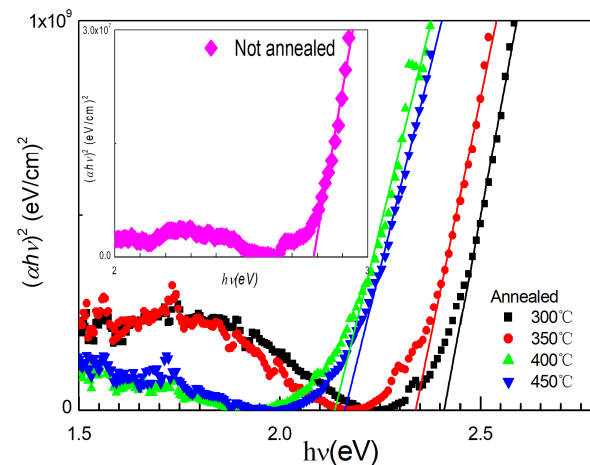


Figure 2. Tauc plots of ZnSnN₂ without annealing or annealed at 300–450 °C.

Hall effect measurements were conducted, and the results of the samples are listed in Table 1. The samples without annealing are almost insulating, and the resistivity is beyond the measurement scope of the Hall effect instrument. The samples without annealing are still *n*-type conductive since their Seebeck coefficients *S_e* were measured to be negative [21], and no reversal in the conduction type is observed here. After being annealed at 300–450 °C, the samples turn conductive. The electron density *n* of the samples annealed at 300 °C is $5.54 \times 10^{17} \text{ cm}^{-3}$ and this is much lower than *N_c*, the room temperature density of the states of the conduction band of ZnSnN₂ ($1.04 \times 10^{18} \text{ cm}^{-3}$) [4,14]. The gap between the conduction band minimum *E_c* and the Fermi level *E_F* was calculated to be 0.0165 eV with

$$n = N_c \exp[-(E_c - E_F)/(kT)], \quad (2)$$

where *k* is the Boltzmann constant and *T* is the absolute temperature (300 K here). The electron density increases to $\sim 10^{18} \text{ cm}^{-3}$ when the annealing temperature is 350, 400 or 450 °C. The mobility is similar to that of the amorphous and microcrystalline samples deposited by reducing the Zn/Sn ratio [13].

Table 1. The mobility μ ($\text{cm}^2\text{V}^{-1}\text{s}^{-1}$) and carrier concentration *n* (cm^{-3}) of the samples annealed at 300–450 (°C) (The resistivity of the samples without annealing is beyond the scope of the instrument).

°C	μ ($\text{cm}^2\text{V}^{-1}\text{s}^{-1}$)	<i>n</i> (cm^{-3})
300	0.988	5.34×10^{17}
350	5.54	8.37×10^{18}
400	2.96	6.48×10^{18}
450	1.22	8.11×10^{18}

To reveal the microscopic change of the structure, the samples without annealing and the samples annealed at 300 °C were studied with TEM (Figure 3). Crystallites with a size slightly larger than 2 nm can be observed, and no diffraction patterns are observed in the samples without annealing (Figure 3a). The fact that no diffraction patterns are observed possibly results from the fact that the density of the crystallites or the volume ratio of the crystalline component to the amorphous component is small (Figure 3a). After being

annealed at 300 °C, crystallites with bigger sizes, larger densities and diffraction spots are observed in the high-resolution image and diffraction patterns, and the sizes of the crystallites are 5–10 nm (Figure 3b). Annealing is found to increase the size of crystallites. In amorphous Si with crystallites smaller than 20 Å, a reversal in the conduction type can be observed in the Hall effect measurement [22,23]. The fact that no reversal in the conduction type is observed in the Hall effect measurement of our samples very possibly results from the nanocrystalline grains, which provide limited long-range order [22].

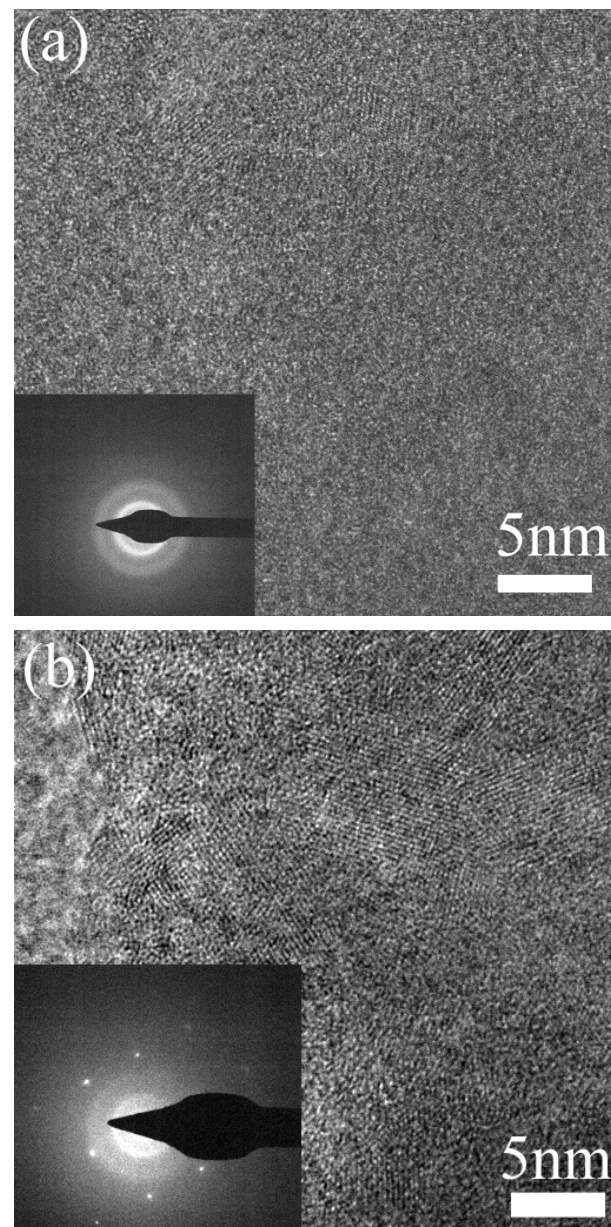


Figure 3. TEM images and the diffraction patterns of ZnSnN₂. (a) Without annealing; (b) annealed at 300 °C.

The AFM images of the samples fabricated at 50 °C, 100 °C, 250 °C and 300 °C and at 35 W are presented in Figure 4. The root mean square (RMS) roughness of the samples deposited at 50 °C, 100 °C, 250 °C and 300 °C is 0.77 nm, 1.27 nm, 0.92 nm and 2.35 nm, respectively. The amorphous samples deposited at 50 °C are found to have the lowest RMS roughness. The morphology of polycrystalline samples is similar to those obtained by others [24].

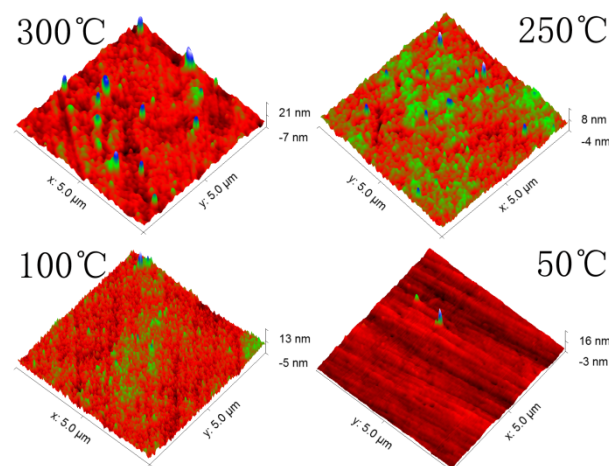


Figure 4. AFM images of the ZnSnN₂ samples deposited at 35 W under different substrate temperatures.

The samples were measured with XPS. A survey in 0–1400 eV shows that the samples contain Zn, Sn and N, together with adventitious O. The high-resolution binding energy spectra of Zn, Sn, N and O of the samples without annealing and those annealed at 300 °C are presented in Figure 5a,b.

For the ZnSnN₂ samples without annealing, Zn 2p_{3/2} and Zn 2p_{1/2} are at 1021.38 and 1044.45 eV, while for the ZnSnN₂ samples annealed at 300 °C, these peaks shift to 1021.57 and 1044.64 eV. Therefore, Zn is at +2 [24]. The peak at approximately 498 eV present in the Sn spectrum is due to the Zn L_{3M45M45} Auger peak [4,25]. Sn is at +4 since Sn 3d_{5/2} and 3d_{3/2} are at 486.11 and 494.52 before annealing, and these peaks shift to 486.18 and 494.58 after annealing [13,24]. In the high resolution XPS spectrum of N 1s, a peak at approximately 403 eV is observed and it is from absorbed γ -type nitrogen molecules labeled as γ -N₂ (N \equiv N). The possible origin of γ -N₂ is nitrogen molecules, which are not decomposed but absorbed directly during sputtering [26,27]. The peak below 400 eV can be deconvoluted into two peaks. In the samples without annealing, the two N 1s peaks are at 396.31 and 397.80, and they shift to 396.90 and 398.35 eV after annealing. The lower energy peak with a much stronger intensity at 396.31 and 396.90 eV implies nitrogen is at –3, while the weaker higher energy peak at 397.80 and 398.35 eV is from organic nitrogen [7,13].

The O 1s peak can also be decomposed into two peaks. The peaks of the samples without annealing are at 529.90 and 531.18 eV, and after annealing, the peaks shift to 529.99 and 530.58 eV. The exact origin of the oxygen present in ZnSnN₂ is still under debate. Some researchers think that the oxygen present in ZnSnN₂ is completely from post-deposition adsorption in air [7]. In our work, we think that the oxygen has two possible origins: the low energy peak is possibly from residual oxygen in the sputtering chamber, which was incorporated during sputtering and which substitutes nitrogen in the lattice [13]; the high energy peak is due to post-deposition adsorption in air.

The atomic ratio of Zn to Zn + Sn is 0.80 before annealing and 0.78 after annealing. In the literature, ZnSnN₂ samples with Zn/(Zn + Sn) = 0.72 and an electron density of $2.7 \times 10^{17} \text{ cm}^{-3}$ were reported [5]. The decrease is mainly due to the loss of Zn, since Zn has much higher vapour pressure than Sn at the annealing temperature of 300 °C. Most possibly, Sn atoms, which substitute the positions of Zn atoms, are the major donors in these nanocrystalline samples, and this is similar to its polycrystalline or crystalline counterpart [18,19].

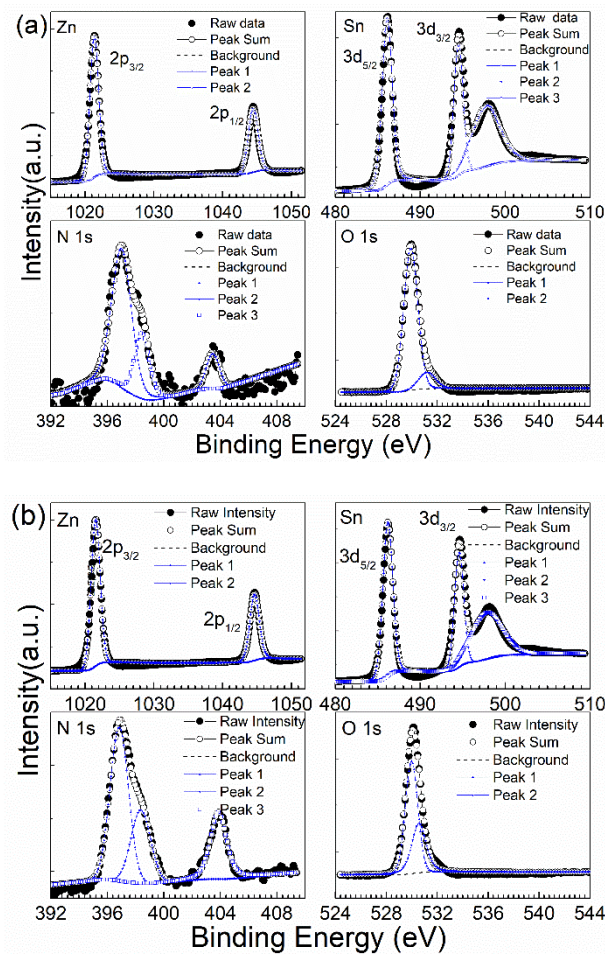


Figure 5. High resolution binding energy peak of Zn, Sn, N and O in ZnSnN₂. (a) Without annealing; (b) annealed at 300 °C.

Figure 6 shows the current density J vs. voltage V curves of the Schottky diodes with the structure of Ag\ITO\ZnSnN₂\Ag. The diode is forward-biased when the silver metal directly on the ZnSnN₂ layer is connected with the anode of the voltage. Rectification is observed, and obviously the rectification is from the Schottky contact formed between ZnSnN₂ and Ag since the structure of Ag\ITO\ZnSnN₂\ITO\Ag shows linear JV curves (Supplementary Materials Figure S5). The transport properties of our nanocrystalline ZnSnN₂ very possibly follow those of crystalline semiconductors since the transport behaviour of amorphous and microcrystalline Si with crystallites of or over 20 Å follows that of crystalline Si [22,23], and the crystallite of our nanocrystalline ZnSnN₂ meets this size requirement. In the following, theories or models based on crystalline semiconductors will be used. Under the thermal emission-diffusion model, the current through a Schottky barrier diode at a voltage of V [28,29] is as follows:

$$J = J_s \exp[-\zeta q(V - IR_s)/(kT)] \{ \exp[q(V - IR_s)/(kT)] - 1 \}, \quad (3)$$

where $J_s = I_s/S = A^{**}T^2 \exp[-q\phi_{b0}/(kT)]$, J_s is the current density, I_s is the saturation current at zero bias, S is the diode area (0.10 × 0.10 cm² here), A^{**} is the effective Richardson constant ($A^{**} = 14.40 \text{ A} \cdot \text{cm}^{-2} \cdot \text{K}^{-2}$ for ZnSnN₂ since the Richardson constant A^* for a free electron is $120 \text{ A} \cdot \text{cm}^{-2} \cdot \text{K}^{-2}$, and the effective electron mass of ZnSnN₂ is 0.12 times that of a free electron [14]), q is the elementary charge, ϕ_{b0} is the barrier height at zero bias (the energy needed by an electron at the Fermi level in the metal to enter the conduction band of the semiconductor at zero bias), R_s is the series resistance due to the neutral region of the semiconductors, ζ is a factor without unit, ζ is equal to $1 - \eta^{-1}$, where η is the

ideality factor, and other symbols have the same meaning as in previous formulas. From the forward-biased experimental data, the three unknown parameters ϕ_{b0} , ξ and R_S can be fitted with the least square method, and the results, together with the calculated η , are presented in Figure 6a.

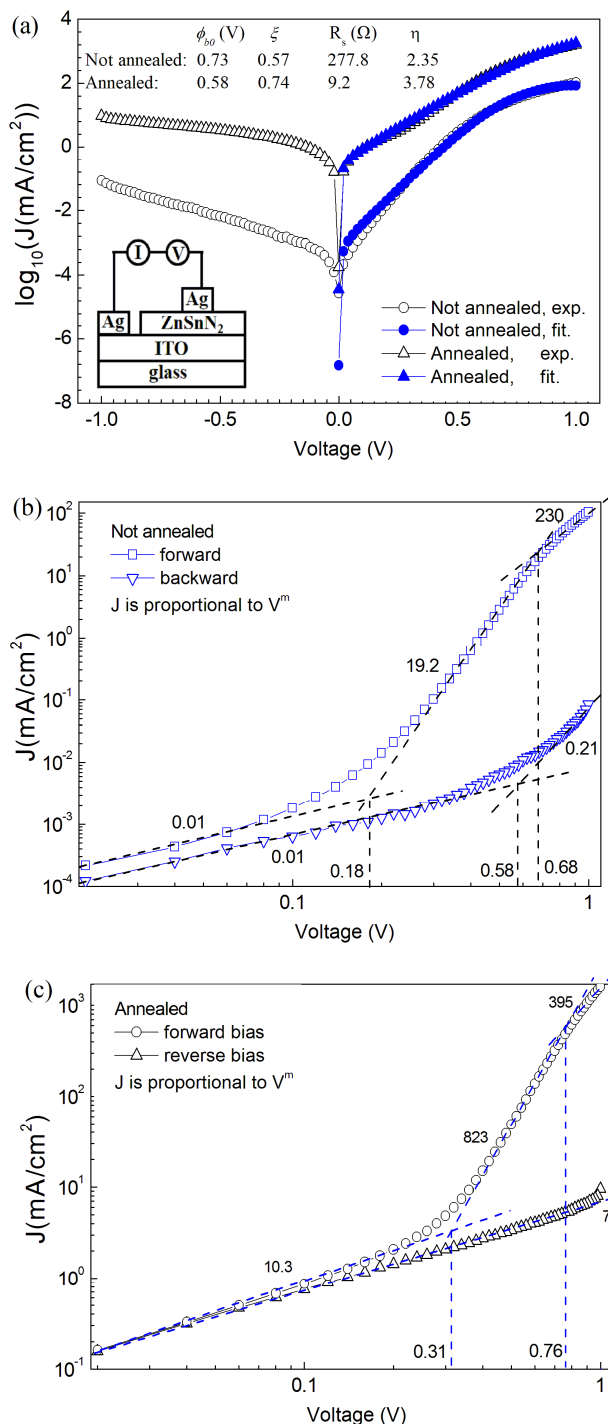


Figure 6. (a) The J – V curves of Ag/ITO/ZnSnN₂/Ag Schottky contact (The Schottky contact is forward-biased when the Ag electrode in direct contact with ZnSnN₂ is connected with the anode of the voltage. The inset shows the structure of the Schottky diodes). (b) $\log J$ – $\log V$ curves of the samples without annealing; (c) $\log J$ – $\log V$ curves of the samples annealed at 300 °C.

At lower forward biased voltages, the fitted current is slightly larger than the experimental data, while good fitting is observed when the forward bias is over ~ 0.3 V in both samples. Since the mobility of both samples is low, diffusion is most likely the major transport mechanism at lower forward biased voltages, and thermal emission becomes obvious with an increase in the forward biased voltage. The fitted series resistance R_s of ZnSnN₂ without annealing is 277.8 Ω , which is larger than that of ZnSnN₂ annealed at 300 °C (9.2 Ω) and this agrees with the fact that the former has poorer conductivity than the latter.

The theoretical Schottky barrier height ϕ_{b0} at zero bias for ideal or intimate Ag-ZnSnN₂ is calculated to be 0.36 eV (the ideal band diagram is shown in Supplementary Materials Figure S6a) since theoretical ϕ_{b0} is equal to $W_m - \chi$, where W_m is the work function of Ag ($W_m = 4.26$ eV for Ag) and χ is the electron affinity of ZnSnN₂ ($\chi = 3.9$ eV for ZnSnN₂ [30,31]). The fitted ϕ_{b0} is larger than the theoretical value, and the Schottky barrier height is enhanced. Schottky barrier height enhancement can result from surface Fermi-level pinning [32], a surface inversion layer (which possibly results from the diffusion of Ag into ZnSnN₂, and Ag atoms substituting Zn or Sn are acceptors) [33,34] or interface oxide states [32]. Surface Fermi-level pinning is less likely here since the forbidden band gap E_g calculated from the fitted ϕ_{b0} will be approximately 1.0 eV (under surface Fermi-level pinning, ϕ_{b0} is equal to $E_g - \phi_0$, where ϕ_0 is the surface neutral energy level measured from the edge of the valence band and is usually approximately $E_g/3$ [32]), which is less than half of those obtained from the Tauc plot. The fact that the calculated ideality factor η is over two also suggests the existence of interface oxide states since the ideality factor of a Schottky diode whose barrier height is enhanced by a surface inversion layer is usually below two [33].

A. M. Cowley and S. M. Sze [32] proposed that when there is interfacial oxide (the band diagram of the Schottky contact with interface states is shown in Supplementary Materials Figure S6b), the Schottky barrier height is expressed as:

$$\phi_{b0} = \gamma(W_m - \chi) + (1 - \gamma)(E_g - \phi_0)/q - \Delta\phi_n \quad (4)$$

and the interface states $D_s = (1 - \gamma)\epsilon_i / (\gamma q^2 \delta)$, where γ is a weighting factor (without unit), $\Delta\phi_n$ is the image force barrier lowering, ϵ_i is the dielectric constant of the interfacial layer, δ is its thickness and other symbols have the same meaning as previously defined. If we suppose $\Delta\phi_n = 0$, $\phi_0 = E_g/3$, where E_g is chosen to be 2.5 eV and ϕ_{b0} = the fitted value, γ will be 0.71 for the samples without annealing and 0.83 for the samples annealed at 300 °C. With the assumption that $\epsilon_i = \epsilon_0$ (free space dielectric constant) and $\delta = 5$ Å [32], the interface states D_s will be 4.42×10^{12} states·eV⁻¹·cm⁻² for the samples without annealing and 2.19×10^{12} states·eV⁻¹·cm⁻² for the samples annealed. The samples without annealing have larger interface states than the samples annealed. The interface states of our samples are in the same magnitude with that of the Al/*n*-Si system (where Si is single-crystalline) [35], but roughly one magnitude smaller than that (3×10^{13} states·eV⁻¹·cm⁻²) of metals and amorphous Si systems which have the same oxide thickness of 5 Å and whose Fermi-level were pinned [36].

Figure 6b,c shows the logarithmic J-V curves of the samples without annealing or annealed at 300 °C. For both samples, both the forward- and reverse-biased data obey the power law ($J \propto V^m$), but m varies in different voltage ranges. For the samples without annealing, below 0.18 V, m is less than one, and this suggests that the current is controlled by the diode. Between 0.18 V and 0.68 V, m is approximately 19.2. After 0.68 V, m is approximately 230. This implies that after 0.18 V, the current is bulk-controlled, and there is an exponential distribution of trap-levels within the forbidden gap of ZnSnN₂. The reverse-biased data of the samples without annealing is diode-controlled since m is below one in the whole measurement range. For the samples annealed at 300 °C, m is well over two in both the forward and backward bias, and this suggests that the current is bulk-controlled, and annealing reduces the resistivity of ZnSnN₂.

Figure 7a,b show the curves of the inverse of the square of the capacitance C (per unit area) vs. voltage V for the samples without annealing or annealed at 300 °C. For

both samples, nonlinear C^{-2} - V curves are observed. The peak in Figure 7b is possibly due to the series resistance [37,38]. Considering the nonlinearity of the C^{-2} - V curves and the fact that the ideality factor η obtained from the IV curves is over two, we think the possibility that the barrier height enhancement results from a surface inversion layer can be excluded [33]. The nonlinearity of the C^{-2} - V curves suggests the existence of excess capacitance. When there is an interfacial layer in the Schottky contact, the capacitance C of a Schottky diode [39] is equal to $[C_i^{-1} + (C_D + C_{ex})^{-1}]^{-1}$, where C_i is the capacitance due to the interfacial layer, C_D is the depletion capacitance of the junction and C_{ex} is the excess capacitance due to surface states or deep traps. For thin interfacial layers, C_i is very large and can be ignored. Therefore, C is equal to $C_D + C_{ex}$. Though C^{-2} vs. V curves are not linear, $(C - C_{ex})^{-2}$ vs. V or C_D^{-2} vs. V will be linear.

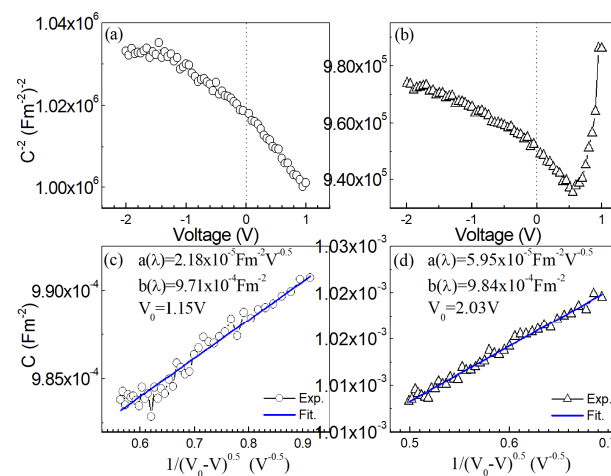


Figure 7. The C^{-2} - V curves of the samples without annealing (a) or annealed at 300 °C (b); $C - (V_0 - V)^{-0.5}$ curves of the samples without annealing (c) or annealed at 300 °C (d).

For the Schottky barrier where there is an oxide between the metal and the semiconductor, J. Szatkowski et al. [40] further proposed that

$$C = a(\lambda)(V_0 - V)^{-0.5} + b(\lambda), \quad (5)$$

where $a(\lambda)$ is $(1 - \lambda + \lambda\gamma)(q\epsilon_0\epsilon_r N_D \gamma / 2)^{-0.5}$, N_D is the doping concentration, $b(\lambda)$ is $\lambda\gamma q^2 D_s$, V_0 and λ are constants, ϵ_r is the relative dielectric constant of ZnSnN₂ ($\epsilon_r = 11$ [20]) and other symbols have the same meaning as in previous formulas. From the data about the capacitance C and reverse-biased voltage V , $a(\lambda)$, $b(\lambda)$ and V_0 can be fitted with the least square method. Both the experimental and fitted capacitance C vs. $(V_0 - V)^{-0.5}$ curves (where only the reverse-biased data are used) of the samples without annealing or with annealing are shown in Figure 7c,d. The fitted $a(\lambda)$, $b(\lambda)$ and V_0 are also presented in Figure 7c,d. As can be seen from Figure 7c,d, the relation between the capacitance C and $(V_0 - V)^{-0.5}$ is indeed linear.

If N_D is known, λ can be calculated from $a(\lambda)$ and then D_s from $b(\lambda)$, since γ has been obtained from the JV curves, and $a(\lambda)$ and $b(\lambda)$ have been obtained from the CV curves. For the samples annealed at 300 °C, λ and D_s are calculated to be 5.86 and 1.25×10^{11} states·eV⁻¹·cm⁻² if we suppose that $N_D = n = 5.34 \times 10^{17}$ cm⁻³. The samples without annealing are almost insulating, and we can suppose that $N_D = 10^{15}$ cm⁻³ [36]. λ and D_s are then calculated to be 2.49 and 3.40×10^{11} states·eV⁻¹·cm⁻². The interface states extracted from the capacitance-voltage of the samples without annealing are larger than those of the samples annealed at 300 °C, and this is in agreement with that obtained from I - V curves.

In addition, the interface states extracted from the C - V curves are roughly one-magnitude smaller than those from the J - V curves. The J - V and C - V curves of the Schottky diodes formed between nanocrystalline ZnSnN₂ and Ag are found to follow the theories

based on crystalline semiconductors, in agreement with amorphous or microcrystalline Si with crystallites between 20–130 Å [22,23].

Figure 8a shows the current density J vs. the voltage V curves of the Ag\ITO\Cu₂O\ZnSnN₂\Ag and Ag\ITO\Cu₂O\ZnSnN₂\Au heterojunction solar cells under the illumination of AM1.5. The only difference between the two solar cells is that the electrode in connection with ZnSnN₂ is Ag for one solar cell and Au for the other. The open-circuit voltage V_{oc} (V), short-circuit current density J_{sc} (mA/cm²), fill factor FF and power conversion efficiency PCE (%) are listed in the inset. The statistical distribution of these solar cells is presented in Figure S7 (the statistics are based on nine samples for the Ag\ITO\Cu₂O\ZnSnN₂\Au solar cell, while the statistics are based on eight samples for the Ag\ITO\Cu₂O\ZnSnN₂\Ag solar cell). The average V_{oc} , J_{sc} , FF and PCE of the solar cell with Au as the electrode are 0.22 V, 1.75 mA/cm², 42% and 0.15%, while those of the solar cell with Ag as the electrode are 0.19 V, 0.34 mA/cm², 22% and 0.02%, respectively. When the electrode in connection with ZnSnN₂ changes from Ag to Au, the four parameters increase greatly, implying better device performance. The measured series resistance of the solar cell with Au as the electrode is 0.83 kΩ, and that with Ag as the electrode is 4.19 kΩ. The improvement in performance mainly results from the change in the electrode. Previous work shows that Au can react with Sn to form AuSn even at room temperature, and the contact between AuSn and n -type GaAs is ohmic [41]. Though the contact between Au and ZnSnN₂ is theoretically non-ohmic (the work function of Au is 5.1 eV and the Fermi level of Au is much lower than that of ZnSnN₂), the Au electrode was thermally evaporated, and it is possible that there are interfacial alloys formed such as AuSn that reduce the Au-ZnSnN₂ contact resistance greatly.

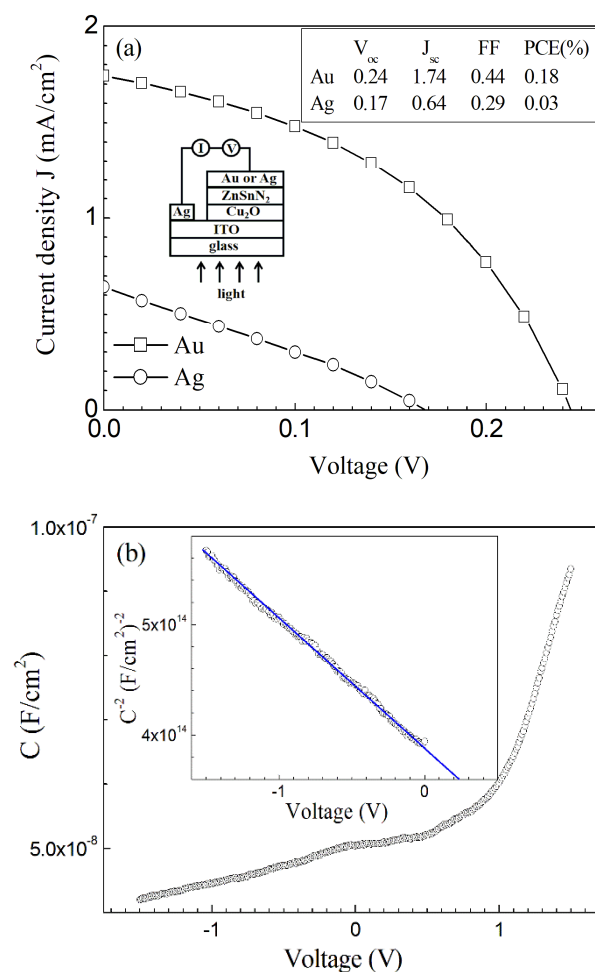


Figure 8. Cont.

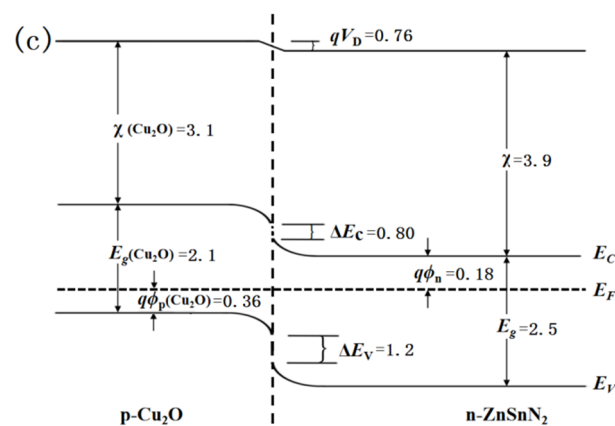


Figure 8. (a) The current density J vs. the voltage V curves of the Ag\ITO\Cu₂O\ZnSnN₂\Ag and Ag\ITO\Cu₂O\ZnSnN₂\Au solar cells (the inset shows the structure of these heterojunction solar cells); (b) the CV curve of the Ag\ITO\Cu₂O\ZnSnN₂\Au solar cell; (c) the energy band diagram of Cu₂O–ZnSnN₂ heterojunction at zero bias.

Figure 8b shows the capacitance C -Voltage V curve of the Ag\ITO\Cu₂O\ZnSnN₂\Au heterojunction solar cell (measured under darkness), with the inset showing the C^{-2} - V curve under reverse bias. It can be found that C^{-2} - V in the reverse bias is linear, and the intercept between the C^{-2} - V line and the voltage axis is approximately 0.24 V. This suggests that Cu₂O-ZnSnN₂ heterojunction is abrupt, with a built-in potential of 0.24 V. The built-in potential of 0.24 V is very near to the average open-circuit voltage (0.22 V) of the solar cell with Au as the electrode. Figure 8c shows the energy band diagram of the Cu₂O-ZnSnN₂ heterojunction at zero bias. The diagram shows a staggered, type II heterojunction. The built-in potential V_D , conduction band and valence band discontinuities, ΔE_c and ΔE_v , are estimated to be 0.76 V, 0.80 eV and 1.2 eV, respectively (Supplementary Materials Figure S8). The obtained V_{oc} needs great improvement as compared with V_D . The presence of the conduction band and valence band discontinuities, ΔE_c and ΔE_v , accounts partially for the low PCE.

In addition, after being stored in air without encapsulation for 11 months, the JV curves of the Ag\ITO\Cu₂O\ZnSnN₂\Au solar cells were measured under the AM1.5 illumination and the average V_{oc} , J_{sc} , FF and PCE (%) were 0.06 V, 0.56 mA/cm², 27% and 0.01%, respectively (the statistical data obtained after the storage for 11 months are also presented in Figure S7). The performance degradation might be due to the storage in air without encapsulation. Though all performance factors decrease as compared with those obtained 11 months ago, the photovoltaic effect still exists.

Figure 9a shows the dark JV curve on a log-log scale for the Ag\ITO\Cu₂O\ZnSnN₂\Au heterojunction. The forward-biased JV curve obeys the power law ($J \propto V^m$) with different exponent values m at different voltage ranges (the junction is forward-biased when the electrostatic potential of Cu₂O is higher than that of ZnSnN₂). In 0–0.19 V, m is smaller than unity, implying that the current is controlled by the heterojunction diode. This also suggests that the resistance of the heterojunction is not large, since large resistance usually results in ohmic behaviour under relatively low voltage. In 0.19–0.98 V, m is approximately two while over 0.98 V m is over three. This implies that the regime in 0.19–0.98 V is the trap-filled limited (TFL) region where only partial traps are filled and the current is due to a space charge limited current (SCLC) [42]. In the region over 0.98 V, all the traps are filled, strong injection happens and the current increases sharply with an increase in the voltage. If we suppose that V_{tr} (0.19 V in Figure 9a) is the turn-on voltage at which the space charge limited conduction takes place in ZnSnN₂ and V_{TFL} (0.98 V in Figure 9a) is the voltage required to fill the traps of ZnSnN₂, the trap density N_t and the trap energy level E_t are calculated to be $2.14 \times 10^{16} \text{ cm}^{-3}$ and 0.1 eV, since V_{tr} equals $16qnt^2 N_t / \{9\epsilon_r \epsilon_0 N_c \exp[(E_t - E_c)/(kT)]\}$ and V_{TFL} equals $qN_t t^2 / (2\epsilon_r \epsilon_0)$, where n is the

free carrier density ($n = N_D = 10^{15} \text{ cm}^{-3}$), t is the film thickness (236 nm) and the other symbols have the same meaning as previously defined.

The heterojunction parameters, including the diode current J_0 , the ideality factor η , the series resistance R_s and the shunt conductance G can be extracted based on a single diode model [43,44]:

$$J = J_0 \exp\left[\frac{q}{\eta kT}(V - R_s J)\right] + GV - J_L, \quad (6)$$

where J_L is the light-induced current ($J_L = J_{SC} = 1.74 \text{ mA/cm}^2$ here), while the other parameters have the same meaning as previously defined. Figure 9b shows the dJ/dV vs. V curve, and the shunt conductance G is found to be 0.43 mS/cm^2 from the nearly flat area in the reverse bias. The dV/dJ vs. $[J + J_{SC}]^{-1}$ curve is presented in Figure 9c, and the series resistance R_s is calculated to be $1.26 \Omega \cdot \text{cm}^2$. From the $J + J_{SC} - GV$ vs. $V - R_s J$ curve in Figure 9d, the diode current J_0 and the ideality factor η are calculated to be $7.76 \times 10^{-2} \text{ mA/cm}^2$ and 2.90, respectively. The ideality factor η larger than two implies that the current transport is recombination-limited [45]. To improve the conversion efficiency, the series resistance needs to be reduced and the shunt resistance needs to be improved. The possible methods include better ohmic contact, optimum film thickness, etc. The band gap needs to be reduced to improve the short-circuit current density J_{SC} . The theoretical open-circuit voltage V_{oc} of the solar cell is estimated to be 0.24 V since V_{oc} approximately equal $(\eta kT/q) \ln[(J_{sc}/J_0) + 1]$ if the series resistance and shunt resistance are negligible and the photogenerated current equals the short-circuit current density J_{SC} . The diode current J_0 needs to be reduced to further improve the open-circuit voltage V_{oc} .

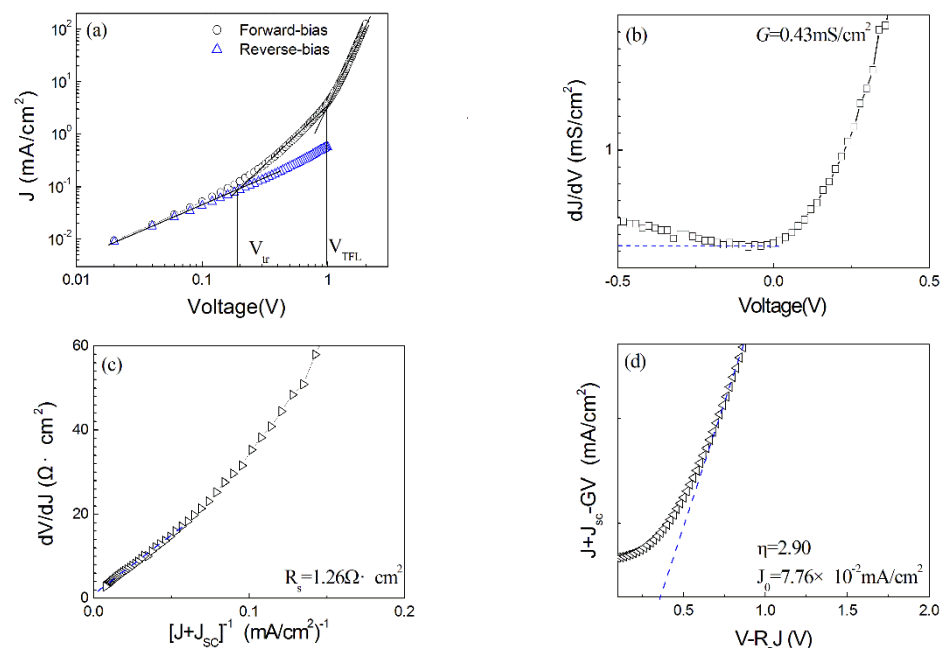


Figure 9. (a) The log–log dark JV curve; (b) dJ/dV vs. V curve; (c) dV/dJ vs. $[J + J_{SC}]^{-1}$ curve; (d) $J + J_{SC} - GV$ vs. $V - R_s J$ curve.

The major structure and power conversion efficiency of several heterojunction solar cells, such as polycrystalline ZnSnN_2 , Si, GaAs, etc [12,30,46–49], are listed in Table 2. The PCE (%) of $\text{Cu}_2\text{O-ZnSnN}_2$ needs great improvement compared with these heterojunction solar cells. The low PCE of $\text{Cu}_2\text{O-ZnSnN}_2$ possibly mainly results from the band gap of nanocrystalline ZnSnN_2 and the energy band diagram of the heterojunction. The band gap of nanocrystalline ZnSnN_2 is approximately 2.5 eV and this is much wider than the optimum band gap to yield the highest PCE (%). A recent report shows that polycrystalline ZnSnN_2 with a band gap of 1.43 eV can be prepared by sputtering under bias [50], and this provides a clue about reducing the band gap of nanocrystalline ZnSnN_2 . One possible

method to reduce the conduction and valence band discontinuities (Figure 8c) is to deposit a buffer between Cu_2O and ZnSnN_2 . Replacing Cu_2O with other *p*-type semiconductors such as CuCrO_2 is another method since theoretical work shows that the PCE (%) of CuCrO_2 - ZnSnN_2 is approximately 22% [2]. ZnSnN_2 belongs to the few solar cell absorption materials that can meet tetra Watt power needs at very low cost, and this necessitates further work in improving its material properties and device performance.

Table 2. The major structure and power conversion efficiency (PCE) of several heterojunction solar cells (pc refers to polycrystalline).

Layer/Stack	PCE (%)
pc- ZnSnN_2 /SnO and pc- ZnSnN_2 / Al_2O_3 /SnO	0.37 [12] and 1.54 [30]
α -C/Si	1.5 [46]
ZnO/ZnGeO/ Cu_2O :Na	8.1 [47]
MXene/GaAs	9.69 [48]
α -Si:H/c-Si	25.6 [49]

4. Conclusions

The reactive preparation and properties of nanocrystalline ZnSnN_2 , together with its Schottky diodes and heterojunction solar cells, were investigated. ZnSnN_2 reactively deposited at 35 W and room temperature is nanocrystalline with crystalline grains of 2 nm. Annealing increases the grain size and the volume ratio of the crystalline component to the amorphous component. Annealing reduces the optical band gap and improves the electrical conductivity of ZnSnN_2 . Nanocrystalline ZnSnN_2 annealed at 300 °C in Ar has an electron concentration of $5.54 \times 10^{17} \text{ cm}^{-3}$ and mobility of $0.998 \text{ cm}^2 \cdot \text{V}^{-1} \cdot \text{s}^{-1}$, which is much better than that of polycrystalline or crystalline ZnSnN_2 , whose electron density in most cases is usually approximately 10^{19} cm^{-3} . The thermal emission-diffusion model was used to analyze the *I-V* curves of the Ag-nanocrystalline ZnSnN_2 Schottky diode. At lower forward biased voltages, diffusion is the major transport mechanism, and thermal emission becomes obvious at higher forward biased voltages. Both the *I-V* and *C-V* curves suggest the existence of interface states, which are calculated to be approximately $10^{12} \text{ states} \cdot \text{eV}^{-1} \cdot \text{cm}^{-2}$ from the *IV* curves and approximately $10^{11} \text{ states} \cdot \text{eV}^{-1} \cdot \text{cm}^{-2}$ from the *CV* curves. Nanocrystalline ZnSnN_2 -based heterojunctions were successfully fabricated. The heterojunction interface is abrupt. The performance of the Ag\ITO\Cu₂O\ZnSnN₂\Au heterojunction solar cell is much better than that of the Ag\ITO\Cu₂O\ZnSnN₂\Ag solar cell. The current transport of the Ag\ITO\Cu₂O\ZnSnN₂\Au solar cell is recombination-limited. The fact that nanocrystallization can greatly reduce the electron density of ZnSnN_2 , the *IV* and *CV* curves of the Schottky contact formed between nanocrystalline ZnSnN_2 and Ag obey the theories based on crystalline semiconductors and nanocrystalline ZnSnN_2 -based heterojunction solar cells are successfully prepared suggest that nanocrystallization can pave a new way for the device application of ZnSnN_2 .

Supplementary Materials: The following supporting information can be downloaded at: <https://www.mdpi.com/article/10.3390/nano13010178/s1>, Figure S1: the schematic diagram to show the fabrication steps for the Schottky diodes and heterojunction solar cells; Figure S2: XRD patterns of the samples deposited at 35 W and different substrate temperatures; Figure S3: XRD patterns of the samples deposited at 50 W and different substrate temperatures; Figure S4: Raman scattering spectra of the samples without annealing or with annealing; Figure S5: *IV* curve of the structure of Ag\ITO\ZnSnN₂\ITO\Ag; Figure S6: the ideal and nonideal band diagram of Ag-ZnSnN₂ at zero bias; Figure S7: the statistical distribution of the solar cell performance parameters; Figure S8: the energy band diagram for the Cu₂O-ZnSnN₂ heterojunction [4,17,24,29,51–53].

Author Contributions: Conceptualization, F.Y. and X.-M.C.; funding acquisition, F.Y. and X.-M.C.; investigation, R.-T.H. and Y.-B.Q.; project administration, F.Y. and X.-M.C.; resources, F.Y., Y.-Z.X., D.-P.Z., P.F. and X.-M.C.; supervision, F.Y.; validation, F.Y., R.-T.H., Y.-B.Q. and X.-M.C.; writing—

original draft, F.Y., R.-T.H., Y.-B.Q. and X.-M.C.; writing—review and editing, F.Y. and X.-M.C. All authors have read and agreed to the published version of the manuscript.

Funding: This work was financially supported by the Natural Science Foundation of China (No.:61674107), the Shenzhen Municipal Science and Technology Funding of for Innovation (Project No.: 20200812151132002).

Data Availability Statement: The data presented in this study are available upon request from the corresponding author. The data are not publicly available due to privacy.

Conflicts of Interest: The authors declare to have no competing interests.

References

1. Punya, A.; Paudel, T.R.; Lambrecht, W. Electronic and lattice dynamical properties of II-IV-N₂ semiconductors. *Phys. Status Solidi C* **2011**, *8*, 2492–2499. [\[CrossRef\]](#)
2. Laidouci, A.; Aissat, A.; Vilcot, J. Numerical study of solar cells based on ZnSnN₂ structure. *Sol. Energy* **2020**, *211*, 237–243. [\[CrossRef\]](#)
3. Chinnakutti, K.; Panneerselvam, V.; Salammal, S. Ba-acceptor doping in ZnSnN₂ by reactive RF magnetron sputtering: (002) faceted Ba-ZnSnN₂ films. *J. Alloys Compd.* **2021**, *855*, 157380. [\[CrossRef\]](#)
4. Ye, F.; Chen, Q.Q.; Cai, X.M.; Xie, Y.Z.; Ma, X.F.; Vaithinathan, K.; Zhang, D.P.; Fan, P.; Roy, V. Improving the chemical potential of nitrogen to tune the electron density and mobility of ZnSnN₂. *J. Mater. Chem. C* **2020**, *8*, 4314–4320. [\[CrossRef\]](#)
5. Wang, Y.; Ohsawa, T.; Meng, X.; Alnjiman, F.; Pierson, J.; Ohashi, N. Suppressing the carrier concentration of zinc tin nitride thin films by excess zinc content and low temperature growth. *Appl. Phys. Lett.* **2019**, *115*, 232104. [\[CrossRef\]](#)
6. Gogova, D.; Olsen, V.; Bazioti, C.; Lee, I.; Vines, L.; Kuznetsov, A. High electron mobility single-crystalline ZnSnN₂ on ZnO (0001) substrates. *CrystEngComm* **2020**, *22*, 6268–6274. [\[CrossRef\]](#)
7. Alnjiman, F.; Diliberto, S.; Ghanbaja, J.; Haye, E.; Kassavetis, S.; Patsalas, P.; Gendarme, C.; Bruyère, S.; Cleymand, F.; Miska, P.; et al. Chemical environment and functional properties of highly crystalline ZnSnN₂ thin films deposited by reactive sputtering at room temperature. *Sol. Energy Mater. Sol. Cells* **2018**, *182*, 30–36. [\[CrossRef\]](#)
8. Shing, A.; Tolstova, Y.; Lewis, N.; Atwater, H. Effects of surface condition on the work function and valence-band position of ZnSnN₂. *Appl. Phys. A-Mater.* **2017**, *123*, 735. [\[CrossRef\]](#)
9. Fioretti, A.; Stokes, A.; Young, M.; Gorman, B.; Toberer, E.; Tamboli, A.; Zakutayev, A. Effects of Hydrogen on Acceptor Activation in Ternary Nitride Semiconductors. *Adv. Electron. Mater.* **2017**, *3*, 1600544. [\[CrossRef\]](#)
10. Chinnakutti, K.; Panneerselvam, V.; Salammal, S. Investigation on structural and optoelectronic properties of in-situ post growth annealed ZnSnN₂ thin films. *Mater. Sci. Semicond. Process.* **2019**, *89*, 234–239. [\[CrossRef\]](#)
11. Qin, R.; Cao, H.; Liang, L.; Xie, Y.; Zhuge, F.; Zhang, H.; Gao, J.; Javaid, K.; Liu, C.; Sun, W. Semiconducting ZnSnN₂ thin films for Si/ZnSnN₂ p-n junctions. *Appl. Phys. Lett.* **2016**, *108*, 142104. [\[CrossRef\]](#)
12. Javaid, K.; Wu, W.; Wang, J.; Fang, J.; Zhang, H.; Gao, J.; Liang, L.; Cao, H. Band Offset Engineering in ZnSnN₂-Based Heterojunction for Low-Cost Solar Cells. *ACS Photonics* **2018**, *5*, 2094–2099. [\[CrossRef\]](#)
13. Wu, X.; Meng, F.; Chu, D.; Yao, M.; Guan, K.; Zhang, D.; Meng, J. Carrier Tuning in ZnSnN₂ by Forming Amorphous and Microcrystalline Phases. *Inorg. Chem.* **2019**, *58*, 8480–8485. [\[CrossRef\]](#)
14. Cai, X.; Wang, B.; Ye, F.; Vaithinathan, K.; Zeng, J.; Zhang, D.; Fan, P.; Roy, V. Tuning the photoluminescence, conduction mechanism and scattering mechanism of ZnSnN₂. *J. Alloys Compd.* **2019**, *779*, 237–243. [\[CrossRef\]](#)
15. Veal, T.; Feldberg, N.; Quackenbush, N.; Linhart, W.; Scanlon, D.; Piper, L.; Durbin, S. Band Gap Dependence on Cation Disorder in ZnSnN₂ Solar Absorber. *Adv. Energy Mater.* **2015**, *5*, 1501462. [\[CrossRef\]](#)
16. Kawamura, F.; Yamada, N.; Imai, M.; Taniguchi, T. Synthesis of ZnSnN₂ crystals via a high-pressure metathesis reaction. *Cryst. Res. Technol.* **2016**, *51*, 220–224. [\[CrossRef\]](#)
17. Quayle, P.; Junno, G.; He, K.; Blanton, E.; Shan, J.; Kash, K. Vapor-liquid-solid synthesis of ZnSnN₂. *Phys. Status Solidi B* **2017**, *254*, 1600718. [\[CrossRef\]](#)
18. Chen, S.; Narang, P.; Atwater, H.A.; Wang, L. Phase Stability and Defect Physics of a Ternary ZnSnN₂ Semiconductor: First Principles Insights. *Adv. Mater.* **2014**, *26*, 311–315. [\[CrossRef\]](#)
19. Pan, J.; Cordell, J.; Tucker, G.J.; Tamboli, A.; Zakutayev, A.; Lany, S. Interplay between composition, electronic structure, disorder, and doping due to dual sublattice mixing in non-equilibrium synthesis of ZnSnN₂:O. *Adv. Mater.* **2019**, *31*, 1807406. [\[CrossRef\]](#)
20. Cao, X.; Kawamura, F.; Ninomiya, Y.; Taniguchi, T.; Yamada, N. Conduction-band effective mass and bandgap of ZnSnN₂ earth-abundant solar absorber. *Sci. Rep.* **2017**, *7*, 14987. [\[CrossRef\]](#)
21. Jones, D.; Spear, W.; Lecomber, P. Transport properties of amorphous-germanium prepared by glow-discharge technique. *J. Non-Cryst. Solids* **1976**, *20*, 259–270. [\[CrossRef\]](#)
22. Spear, W.; Willeke, G.; Le Comber, P. Electronic properties of microcrystalline silicon prepared in the glow discharge plasma. *Physica* **1983**, *117–118*, 908–913.
23. Willeke, G.; Spear, W.; Jones, D.; Le Comber, P. Thermoelectric power, Hall effect and density-of-states measurements on glow-discharge microcrystalline silicon. *Philos. Mag. B* **1982**, *46*, 177–190. [\[CrossRef\]](#)

24. Chinnakutti, K.; Panneerselvam, V.; Salammal, S. Tailoring optoelectronic properties of earth abundant ZnSnN₂ by combinatorial RF magnetron sputtering. *J. Alloys Compd.* **2019**, *772*, 348–358. [[CrossRef](#)]
25. Zatsepin, D.; Boukhvalov, D.; Kurmaev, E.; Zhidkov, I.; Kim, S.; Cui, L.; Gavrilov, N.; Cholakh, S. XPS and DFT study of Sn incorporation into ZnO and TiO₂ host matrices by pulsed ion implantation. *Phys. Status Solidi B* **2015**, *252*, 1890–1896. [[CrossRef](#)]
26. Ye, F.; Zeng, J.; Qiu, Y.; Cai, X.; Wang, B.; Wang, H.; Zhang, D.; Fan, P.; Roy, V. Deposition-rate controlled nitrogen-doping into cuprous oxide and its thermal stability. *Thin Solid Films* **2019**, *674*, 44–51. [[CrossRef](#)]
27. Asahi, R.; Morikawa, T.; Ohwaki, T.; Aoki, K.; Taga, Y. Visible-Light Photocatalysis in Nitrogen-Doped Titanium Oxides. *Science* **2001**, *293*, 269–271. [[CrossRef](#)] [[PubMed](#)]
28. Chand, S.; Kumar, J. Current-voltage characteristics and barrier parameters of Pd₂Si/p-Si (111) Schottky diodes in a wide temperature range. *Semicond. Sci. Technol.* **1995**, *10*, 1680–1688. [[CrossRef](#)]
29. Sze, S.; Ng, K. *Physics of Semiconductor Devices*, 3rd ed.; Wiley Interscience: Hoboken, NJ, USA, 2006; p. 159.
30. Javaid, K.; Yu, J.; Wu, W.; Wang, J.; Zhang, H.; Gao, J.; Zhuge, F.; Liang, L.; Cao, H. Thin Film Solar Cell Based on ZnSnN₂/SnO Heterojunction. *Phys. Status Solidi RRL* **2018**, *12*, 1700332. [[CrossRef](#)]
31. Punya, A.; Lambrecht, W. Band offsets between ZnGeN₂, GaN, ZnO, and ZnSnN₂ and their potential impact for solar cells. *Phys. Rev. B* **2013**, *88*, 075302-1–075302-6. [[CrossRef](#)]
32. Cowley, A.M.; Sze, S.M. Surface States and Barrier Height of Metal-Semiconductor Systems. *J. Appl. Phys.* **1965**, *36*, 3212–3220. [[CrossRef](#)]
33. Eglash, S.J.; Newman, N.; Pan, S.; Mo, D.; Shenai, K.; Spicer, W.; Collins, D.M. Engineered Schottky barrier diodes for themodification and control of Schottky barrier heights. *J. Appl. Phys.* **1987**, *61*, 5159–5169. [[CrossRef](#)]
34. Shannon, J.M. Increasing the effective height of a Schottky barrier using low-energy ion implantation. *Appl. Phys. Lett.* **1974**, *25*, 75–77. [[CrossRef](#)]
35. Turut, A.; Saglam, M.; Efeoglu, H.; Yalcin, N.; Yildirim, M.; Abay, B. Interpreting the nonideal reverse bias C-V characteristics and importance of the dependence of Schottky barrier height on applied voltage. *Phys. B* **1995**, *205*, 41–50. [[CrossRef](#)]
36. Wronski, C.; Carlson, D. Surface states and barrier heights of metal-amorphous silicon Schottky barriers. *Solid State Commun.* **1977**, *23*, 421–424. [[CrossRef](#)]
37. Chattopadhyay, P.; Raychaudhuri, B. Origin of the anomalous peak in the forward capacitance-voltage plot of a Schottky barrier diode. *Solid State Electron.* **1992**, *35*, 875–878.
38. Chattopadhyay, P.; Raychaudhuri, B. Frequency dependence of forward capacitance-voltage characteristics of Schottky barrier diodes. *Solid State Electron.* **1993**, *36*, 605–610. [[CrossRef](#)]
39. Vasudev, P.; Mattes, B.; Pietras, E.; Bube, R. Excess capacitance and non-ideal Schottky barriers on GaAs. *Solid State Electron.* **1976**, *19*, 557–559. [[CrossRef](#)]
40. Szatkowski, J.; Sierański, K. Simple interface-layer model for the nonideal characteristics of the Schottky-barrier diode. *Solid State Electron.* **1992**, *35*, 1013–1015. [[CrossRef](#)]
41. Buene, L.; Jacobsen, S.-T. Room Temperature Interdiffusion in Evaporated Au-Sn Films. *Phys. Scr.* **1978**, *18*, 397. [[CrossRef](#)]
42. Chiu, F.-C. A review on conduction mechanism in dielectric films. *Adv. Mater. Sci. Eng.* **2014**, *2014*, 578168. [[CrossRef](#)]
43. Hegedus, S.; Shafarman, W. Thin-film solar cells: Device measurements and analysis. *Prog. Photovolt Res. Appl.* **2004**, *12*, 155–176. [[CrossRef](#)]
44. Chen, S.; Ishap, M.; Xiong, W.; Shah, U.; Farooq, U.; Luo, J.; Zheng, Z.; Su, Z.; Fan, P.; Zhang, X.; et al. Improved open-circuit voltage of Sb₂Se₃ thin film solar cells via interfacial sulfur diffusion-induced gradient bandgap engineering. *Solar RRL* **2021**, *5*, 2100419. [[CrossRef](#)]
45. Carlson, D.E.; Wronski, C.R. Amorphous silicon solar cell. *Appl. Phys. Lett.* **1976**, *28*, 671–673. [[CrossRef](#)]
46. Li, X.; Zhu, H.; Wang, K.; Cao, A.; Wei, J.; Li, C.; Jia, Y.; Li, Z.; Li, X.; Wu, D. Graphene-On-Silicon Schottky Junction Solar Cells. *Adv. Mater.* **2010**, *22*, 2743–2748. [[CrossRef](#)] [[PubMed](#)]
47. Minami, T.; Nishi, Y.; Miyata, T. Efficiency enhancement using a Zn_{1-x}Ge_x-O thin film as an n-type window layer in Cu₂O-based heterojunction solar cells. *Appl. Phys. Express.* **2016**, *9*, 052301-1–052301-4. [[CrossRef](#)]
48. Zhang, Z.; Lin, J.; Sun, P.; Zeng, Q.; Deng, X.; Mo, Y.; Chen, J.; Zheng, Y.; Wang, W.; Li, G. Air-stable MXene/GaAs heterojunction solar cells with a high initial efficiency of 9.69%. *J. Mater. Chem. A* **2021**, *9*, 16160–16168. [[CrossRef](#)]
49. Masuko, K.; Shigematsu, M.; Hashiguchi, T.; Fujishima, D.; Kai, M.; Yoshimura, N.; Yamaguchi, T.; Ichihashi, Y.; Mishima, T.; Matsubara, N.; et al. Achievement of More Than 25% Conversion Efficiency With Crystalline Silicon Heterojunction Solar Cell. *IEEE J. Photovolt.* **2014**, *4*, 1433–1435. [[CrossRef](#)]
50. Virfeu, A.; Alnjiman, F.; Ghanbaja, J.; Borroto, A.; Gendarme, C.; Migot, S.; Kopprilo, L.; Gall, S.L.; Longeaud, C.; Vilcot, J.-P. Approaching Theoretical Band Gap of ZnSnN₂ Films via Bias Magnetron Cosputtering at Room Temperature. *ACS Appl. Electron. Mater.* **2021**, *3*, 3855–3866. [[CrossRef](#)]
51. Quayle, P.C.; He, K.; Shan, J.; Kash, K. Synthesis, lattice structure, and band gap of ZnSnN₂. *MRS Commun.* **2013**, *3*, 135–138. [[CrossRef](#)]

52. Quayle, P.C.; Blanton, E.W.; Punya, A.; Junno, G.T.; He, K.; Han, L.; Zhao, H.; Shan, J.; Lambrecht, W.R.L.; Kash, K. Charge-neutral disorder and polytypes in heterovalent wurtzite-based ternary semiconductors: The importance of the octet rule. *Phys. Rev. B* **2015**, *91*, 205207. [[CrossRef](#)]
53. Meyer, B.K.; Polity, A.; Reppin, D.; Becker, M.; Hering, P.; Klar, P.J.; Sander, T.; Reindl, C.; Benz, J.; Eickhoff, M.; et al. Binary copper oxide semiconductors: From materials towards devices, *Phys. Status Solidi B* **2012**, *249*, 1487–1509. [[CrossRef](#)]

Disclaimer/Publisher’s Note: The statements, opinions and data contained in all publications are solely those of the individual author(s) and contributor(s) and not of MDPI and/or the editor(s). MDPI and/or the editor(s) disclaim responsibility for any injury to people or property resulting from any ideas, methods, instructions or products referred to in the content.